Imaging and Raman Spectroscopy of Individual Single-Wall Carbon Nanotubes on a Large Substrate

5 AUTHORS, INCLUDING:

Stephen O'Brien

City College of New York

126 PUBLICATIONS   **7,797** CITATIONS

Imaging and Raman Spectroscopy of Individual Single-Wall Carbon Nanotubes on a Large Substrate

Li Zhang,[†] Zhang Jia,[‡] Limin Huang,[‡] Stephen O'Brien,[‡] and Zhonghua Yu*,[†]

Department of Chemistry, City College of New York, New York, New York 10031, and Department of Applied Physics & Applied Mathematics, Columbia University, New York, New York 10027

Received: April 13, 2007

A beam-scanning confocal Raman microscope system capable of large-area imaging is developed for characterizing single-wall carbon nanotubes at the single tube level. Individual ultralong nanotubes grown on a large silicon substrate are systematically imaged by both confocal Raman microscopy and scanning electron microscopy. Raman spectra for more than 200 nanotubes, consisting of both semiconducting and metallic nanotubes, are obtained. A large variation in the nanotube radial breathing mode (RBM) Raman intensity is observed for different tubes and can be understood in terms of resonance enhancement and nanotube structure-dependent electron−phonon coupling strength. Nanotube diameters determined from RBM frequencies reveal a broad distribution from 0.8 to ∼2 nm for nanotubes grown by chemical vapor deposition. The tangential mode (G band) Raman spectra of individual metallic nanotubes are found to exhibit a variety of different line shapes, with the Breit−Wigner−Fano feature diminished for most of the observed spectra.

Introduction

Single-wall carbon nanotubes (SWNTs), with a typical diameter of $1-2$ nm and a length ranging from hundreds of nanometers to exceeding 1 mm,[1,2] can be viewed as seamless cylinders wrapped from a graphene sheet. Indicated by the (n, m) indices, the manner in which a graphene sheet is wrapped determines the properties of the resulting nanotubes.[3,4] Nanotubes with similar diameters may be either metallic or semiconducting, and variation of the nanotube diameter leads to dramatic change in SWNT electronic transition energies.[3,4] SWNTs are unique one-dimensional materials with many promising applications including field-effect transistors,[5−7] light-emitting diodes,[7−9] sensors,[10−13] and biological imaging agents.[14−17]

The structure-dependent variation of the electronic properties can be advantageous for potential applications of SWNTs. At the same time, it poses a significant challenge for the characterization of SWNTs, since the current synthesis methods lack control over the physical structures of produced nanotubes. Bulk SWNT samples always consist of a mixture of nanotubes with different diameters and different electronic properties. Single nanotube characterization is therefore important in understanding the structure-dependent properties of nanotubes and in developing nanodevices consisting of individual nanotubes.

Recent progress in catalytic chemical vapor deposition (CVD) synthesis enables the growth of ultralong and oriented arrays of individual nanotubes on various substrates.[1,2,18−20] Individual ultralong tubes and their oriented arrays not only provide a desirable sample for single nanotube characterization but also can generate many new applications that cannot be achieved with short or random network of nanotubes.[21−23] Single nanotube Raman imaging and spectroscopy, a fast and effective method for characterizing the as-grown individual nanotubes

regarding their physical structure, diameter distribution, and relative populations of metallic and semiconducting nanotubes, may provide clues to SWNTs growth mechanism and controlling their uniformity.

In order to characterize SWNTs at the single tube level, it is necessary to identify and follow individual nanotubes precisely. Scanning electron microscopy (SEM) and atomic force microscopy (AFM) have both been routinely used to image nanotubes, but only very limited structural information can be obtained from these two imaging methods. SEM cannot give precise structural determination of individual nanotubes on Si/SiO_2 wafers due to the charging effect.[24] It is also difficult to map individual tubes on a large-area sample by AFM, yet nanotube-based devices often carry such geometries.

Resonant Raman spectroscopy (RRS) has proved to be a powerful tool in the study of the electronic, vibrational, and structural properties of SWNTs.[25−29] The two main Raman-active features of SWNTs are the radial breathing mode (RBM) at low frequency around 200 cm^{-1} and the high-frequency tangential mode (G band) at ∼1590 cm^{-1} associated with C−C stretching. The RBM has been used to determine the tube diameter d_t and relative populations of different diameter nanotubes in a bulk sample because RBM frequency ω_{RBM} is inversely proportional to the tube diameter (but not chirality).[26,30,31] Optical transition energies E_{ii} have been determined from RBM resonance Raman excitation profile[32,33] and RBM anti-Stokes/Stokes Raman intensity ratio.[34−36] Both d_t and E_{ii} can be used to assign (n, m) indices to the observed Raman peaks. On the other hand, the Raman spectral line shape of the G band has been shown to strongly depend on the electronic type of the nanotube. Metallic tubes exhibit broadened G-band Raman spectra, often with an asymmetric Breit−Wigner−Fano (BWF) line shape,[25,37−39] which is in contrast to the sharp Lorentzian line shape for semiconducting tubes. Raman spectroscopy of individual nanotubes, enabled by the strong resonance enhancement effect,[34,40,41] has become an important nondestructive characterization tool to study the structure-

* Corresponding author: e-mail zyu@sci.ccny.cuny.edu.
† City College of New York.
‡ Columbia University.

Imaging and Raman Spectroscopy of Individual SWNTs

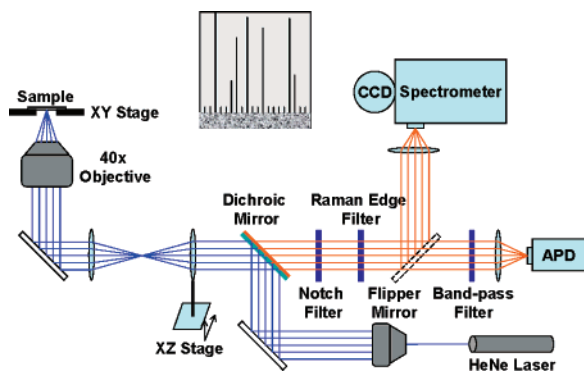*J. Phys. Chem. C, Vol. 111, No. 30, 2007* **11241**

Figure 1. Schematic diagram of the beam-scanning confocal Raman microscope. (Inset) Typical geometry of nanotubes sample grown on a Si substrate by catalytic chemical vapor deposition.

dependent properties of ultralong nanotubes on a substrate[41−43] and even nanotubes underneath a dielectric layer.[44]

In this paper, we describe a beam-scanning confocal Raman microscopy system developed for single nanotube Raman characterization. It was used to map SWNTs grown on large Si/SiO$_2$ substrates of ∼10 mm lateral dimension. We compare Raman imaging with SEM imaging of the same sample to illustrate the imaging capability of our Raman microscopy system. Raman spectra for more than 200 ultralong nanotubes are collected by this imaging technique. Variations in RBM Raman intensity and G-band Raman line shape of individual nanotubes are observed and discussed. Nanotube diameters determined from RBM frequencies generate a broad diameter distribution ranging from 0.8 to ∼2 nm for CVD grown nanotubes.

Experimental Section

Synthesis of Single-Wall Carbon Nanotubes. Samples consisting of oriented individual carbon nanotubes used in this study were grown by controlled chemical vapor deposition with ethanol as carbon source and Co thin film as catalyst, as described previously.[19] Briefly, Co ultrathin films (0.5−2 nm) were deposited on silicon wafers with a ∼200 nm SiO$_2$ layer via e-beam evaporator (Semicore SC2000) with a deposition rate of 0.01 nm/s. A glass slide was used as a mask to deposit Co on only one edge of the substrate. The substrate was then placed in the CVD quartz tube and was gradually heated to 850 °C in an Ar/H$_2$ (520 sccm/65 sccm) flow for 1 h before ethanol was introduced for nanotube growth. During the heating process, the as-deposited Co ultrathin film is believed to ball up to form individual nanoparticles (2−10 nm in diameter). In typical CVD growth, ethanol with a trace amount of water (0.2−5 wt %) was delivered into the CVD reactor by bubbling Ar/H$_2$ mixture gas (10:1 by volume, 60−300 sccm) through an ethanol pool (0 °C). Ultralong nanotubes were found to grow from Co film along the gas flow direction.[2] The sample geometry is shown schematically in the inset to Figure 1. A representative SEM image of an oriented array of isolated ultralong nanotubes grown by this CVD method is shown in Figure 2.

Raman Imaging and Spectroscopy. A laboratory-designed confocal microscope was used for Raman imaging and spectroscopy measurement at the single nanotube level. The microscope is based on a beam-scanning scheme, as shown schematically in Figure 1. The 633 nm excitation laser was focused to a spot of ∼800 nm in size on the sample plane by a microscope objective (Nikon 40×, NA 0.6). Raman scattering signal was collected by the same objective, transmitted through
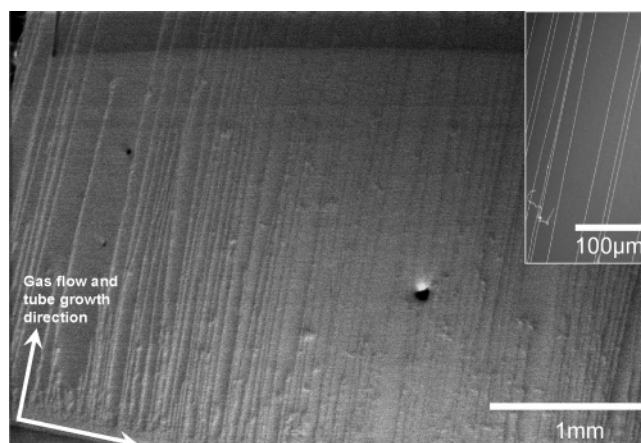

Figure 2. SEM image of an oriented array of SWNTs grown along the gas flow direction from the patterned catalyst on a Si chip. (Inset) Higher magnification image of nanotubes on the Si chip.

the dichroic beamsplitter, and detected by an avalanche photodiode (Perkin-Elmer SPCM-AQR-15). Laser Rayleigh scattering and the Si substrate background Raman scattering were blocked by using a notch filter (Kaiser), a Raman edge filter (Semrock), and a band-pass filter (Andover 700FS10) centered at the SWNTs G-band Raman peak. To image nanotubes, the focused laser spot was raster-scanned over the sample plane by continuously translating the lens close to the dichroic beamsplitter in the plane perpendicular to the optical axis. Because of the magnification of the microscope objective, the translation stage (Melles Griot, Nanomover) used to move the scanning lens does not need a high resolution. A translating repeatability of 1 μm for the stage implies a laser positioning repeatability of 25 nm on the sample plane if a 40× objective is used. This high repeatability allows for fast laser spot positioning to a single nanotube after the Raman image is acquired. Typical scan area was 100 μm × 100 μm, and the integration time was 15 ms for each step. The sample was mounted on a mechanical translational stage so that the sample could be scanned systematically and sequentially across the entire substrate edge near the deposited catalyst. Raman spectra of imaged SWNTs were measured by a liquid nitrogen-cooled CCD camera (Princeton Instruments, Spec-10) attached to the spectrograph (Acton SP2300), with typical exposure times of 3−5 min. The excitation laser power was kept ≤3 mW to avoid laser heating. The entire imaging and positioning process was controlled by Labview software (National Instrument).

The ultralong nanotubes protruding from the catalyst region are the focus of this study. The sample was positioned in such a way that the long nanotubes were perpendicular to the fast scanning axis. Only a few scans starting from the catalyst film were necessary in order to determine whether any ultralong nanotubes were present in the Raman imaging. By this strategy we systematically imaged the large area along the catalyst film, typically 5−10 mm long, on four samples. More than 200 isolated SWNTs that satisfy resonance Raman conditions were imaged and mapped from these four samples in this manner.

SEM Imaging. Scanning electron microscopic images of SWNTs grown on Si/SiO$_2$ substrate were taken on a Hitachi S4700 field emission SEM operated at 0.8 kV. A series of images of ∼200 μm × 100 μm area were taken consecutively along the catalyst region across the substrate, which were subsequently compared to the corresponding Raman images.
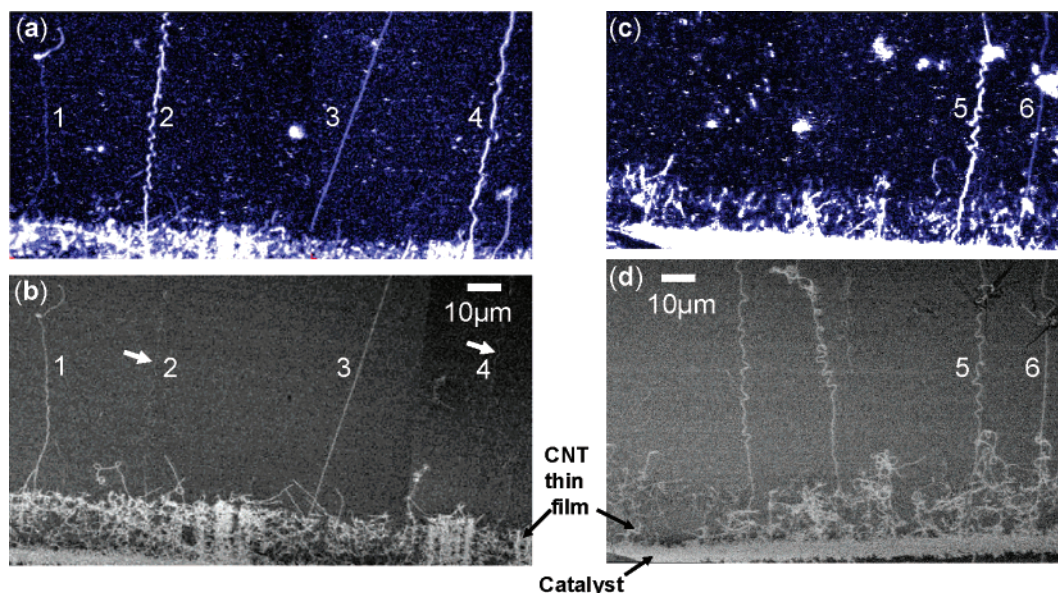
Figure 3. Comparison of Raman and SEM imaging of same sample areas. Raman images were taken with 633 nm excitation wavelength. (a) Raman image and (b) SEM image of one area. The arrows in panel b point to two ultralong nanotubes barely observable in the SEM image. (c) Raman image and (d) SEM image of another area.

Results and Discussion

1. **Combined Raman and SEM Imaging.** Raman imaging of SWNTs was performed prior to SEM imaging to avoid potential damage to SWNTs from excessive exposure to electrons in SEM imaging that might influence the Raman spectra. On each sample, as shown in Figure 3, three regions of variable nanotube growth density can be identified. The catalyst region yields the strongest intensity in Raman imaging, due to the presence of high-density nanotubes and possible photoemission from the catalyst. Next to the catalyst area is the nanotube thin film region consisting of short entangled nanotubes, from which well-separated ultralong nanotubes are seen to protrude. We focus our imaging and Raman spectra measurement on these isolated ultralong tubes.

Using the irregular features in the catalyst area and the nanotube thin film region as markers, we are able to match all the Raman images to the corresponding SEM images of the same area. Figure 3 shows both Raman and SEM images of two representative areas on a sample. In one area, all four nanotubes seen in the SEM image, shown in Figure 3b, can also be identified in the Raman image in Figure 3a. In fact, tubes 2 and 4 are weak and barely observable in SEM imaging, but they appear to be intense in Raman imaging. For another area shown in Figure 3c,d, at least four long tubes are visible in the SEM image, but only two of them, tubes 5 and 6, are revealed in the Raman image, apparently due to the resonance enhancement condition for observing single tube Raman scattering. Raman imaging can reveal only those nanotubes whose electronic transition energies E_{ii} are in resonance with the incident or scattered photons. Careful examination of both SEM and Raman images for all four samples, consisting of more than 200 individual nanotubes, shows that about 60% of the ultralong tubes seen in SEM imaging also appear in G-band Raman imaging under 633-nm excitation.

In our experiment the excitation laser polarization was adjusted to be along the nanotube axial direction in order to achieve maximum Raman intensity.[45-47] In Figure 3a,c, straight nanotubes like tube 3 show uniform Raman intensity along the tube length, as expected from the excitation polarization dependence of SWNTs Raman scattering. On the other hand,
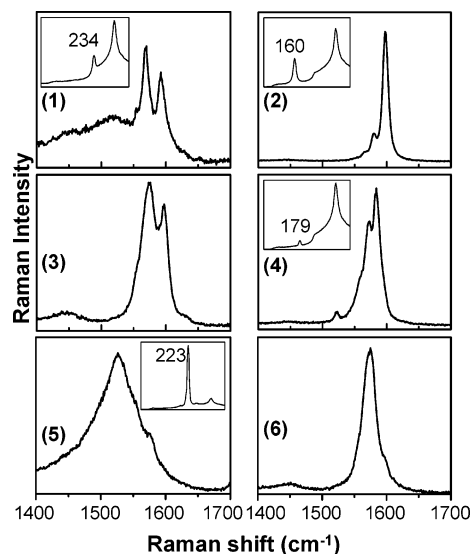

Figure 4. G-band Raman spectra for ultralong nanotubes labeled 1−6 in Figure 3. (Insets) Corresponding RBM features. Tubes 3 and 6 do not display RBM peaks with 633 nm excitation.

the twisted nanotubes, such as tubes 2 and 5, are observed to display variable Raman intensity along their tube length, due to the variation in angle between laser polarization and the nanotube axis direction.

2. **RBM Raman Spectra of Individual SWNTs.** Because RBM and G-mode have different resonance windows, not all nanotubes appearing in G-band Raman imaging display RBM peaks. Among ∼200 individual tubes imaged by G-band Raman scattering, only 95 tubes exhibit RBM modes, consisting of both metallic and semiconducting tubes. The Raman spectra for tubes 1−6 highlighted in Figure 3 are shown in Figure 4. In this case, tubes 3 and 6 do not exhibit RBM peaks under 633-nm laser excitation. Tube 2 shows a typical semiconducting-type G-mode Raman spectrum with relatively sharp Lorentzian line shape. The other five tubes show metallic-type G-mode Raman spectra, with different extents of line broadening. Among them, tube 5 exhibits an asymmetric broad BWF component at 1526 cm^{-1} in the G-band spectrum.
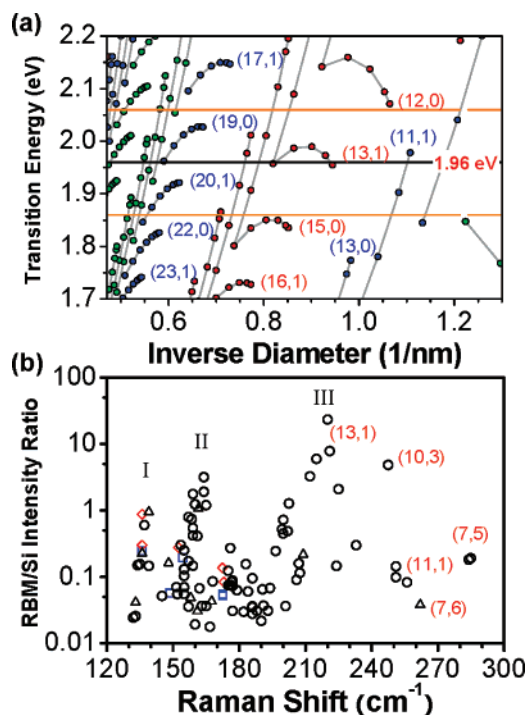
Imaging and Raman Spectroscopy of Individual SWNTs

J. Phys. Chem. C, Vol. 111, No. 30, 2007 **11243**

Figure 5. (a) "Kataura plot" of optical transition energies vs reciprocal diameters of nanotubes. Semiconducting and metallic nanotubes are indicated by different colors (green and blue for semiconducting, and red for metallic). The orange horizontal lines give a resonance window of width ±0.1 eV for excitation energy 1.96 eV (black horizontal line). Some (n, m) indices are also shown on the plot. (b) Normalized RBM intensity vs Raman shift for 95 ultralong nanotubes. I, II, and III indicate three intensity maxima.

For nanotubes showing RBM Raman peaks, the RBM intensity of each nanotube is normalized by the 303 cm^{-1} Raman peak of the Si substrate. Figure 5b displays the normalized RBM intensity for 95 tubes that display RBM features, plotted against their RBM frequencies ω_{RBM}. It can be seen that CVD growth yields nanotubes with a broad diameter distribution, with the observed RBM frequency under 633-nm excitation spanning from at least 135 cm^{-1} up to 285 cm^{-1}. As expected, RBM Raman intensity is observed to generally decrease with increasing nanotube diameter.

To identify the (n, m) chiral indices for these 95 nanotubes, the optical transition energies E_{ii} for different nanotubes are plotted against their inverse diameter in Figure 5a. This plot is adapted from Son et al.,[43] which was calculated by the extended tight-binding (ETB) method[48] and found to agree well with the experimental E_{ii} values for isolated tubes dispersed in water. The transition energies E_{ii} of nanotubes have been shown to depend on the dielectric environment surrounding the nanotubes.[32] Son et al.[49] determined the transition energies for both semiconducting and metallic nanotubes grown on Si by measuring the resonance Raman excitation profile. E_{ii} for tubes on the Si substrate was found to be on average ∼70 meV lower than ETB calculation. Thus the calculated E_{ii} energies have all been downshifted by 70 meV accordingly in Figure 5a. The red circles correspond to metallic tubes, and the green and blue ones correspond to type I [$(2n + m)\mathrm{mod}3 = 1$] and type II [$(2n + m)\mathrm{mod}3 = 2$] semiconducting nanotubes. Due to the trigonal warping effect,[50] the optical transition energy E_{11}^{M} of a non-armchair metallic tube splits to lower energy branch E_{11L}^{M} and high-energy branch E_{11H}^{M}.

It has been established that RBM frequency of a nanotube depends only weakly on its surrounding environment. The RBM

frequencies of nanotubes with the same (n, m) structure have been shown to be very close for tubes dispersed in water, in bundles, or grown on a substrate.[33,51−53] A few equations relating nanotube diameter (d_t) to its RBM frequency ω_{RBM} have been established in literature.[26,52−55] The most recent one by Araujo et al.[53]

$$\omega_{RBM} = 217.8/d_t + 15.7 \qquad (1)$$

is used in the present study to assign (n, m) chiral index to the observed RBM Raman peaks, because this relationship shows agreement for a broad diameter range of nanotubes grown on a quartz substrate (0.7−2.2 nm). Because only a few (n, m) structures are possible within the resonance window for high RBM frequencies (>220 cm^{-1}), these peaks can be assigned satisfactorily by comparison with the predicted RBM frequencies from eq 1. For example, as shown in Figure 5b, the RBM peak at 283 cm^{-1} is assigned to a (7, 5) tube, and the intense 249 cm^{-1} RBM peak is assigned to a (10, 3) tube. They both exhibit sharp semiconducting-type G-band Raman spectra.

Figure 5b also shows that RBM Raman intensity varies periodically with RBM frequency under 633-nm laser excitation, with maxima highlighted by I, II, and III. For intensity maximum III at ∼221 cm^{-1}, the RBM Raman signal is about 10 times stronger than the Si 303 cm^{-1} peak, implying a strong resonance enhancement condition. Its corresponding G-mode Raman spectrum, shown in Figure 4 as tube 5, has a very broad BWF line shape, suggestive of a metallic tube. Among metallic tubes of the family $2n + m = 27$ whose transition energies E_{11L}^{M} are in resonance with the excitation laser, the (13, 1) tube gives a predicted ω_{RBM} of 221 cm^{-1}. The intense RBM peak at 221 cm^{-1} is therefore assigned to (13, 1) structure. The observed RBM frequencies from 221 to 176 cm^{-1} are all assigned to metallic tubes. The electron−phonon (e−ph) coupling matrix element has been predicted to decrease with increasing chiral angle (0° for zigzag tube and 30° for armchair tube).[56,57] This explains the observed decreasing RBM intensity for metallic tubes from 221 cm^{-1} down to ∼190 cm^{-1}. For metallic tubes with ω_{RBM} < ∼190 cm^{-1}, the higher branch of metallic transition E_{11H}^{M} is involved in resonance Raman scattering. The observed RBM Raman intensity for these tubes typically is very weak, consistent with theoretical prediction[58] and other experimental observations[43] regarding Raman scattering involving E_{11H}^{M}.

RBM frequencies <170 cm^{-1} are assigned to large semiconducting tubes within the resonance window under 633-nm excitation, where resonance Raman scattering is associated with the E_{33}^{S} transition. RBM intensity maximum II, at ∼164 cm^{-1}, is assigned to (19, 0) or (18, 2) tubes, which are zigzag-like structure and therefore should have larger e−ph matrix elements. Equation 1 predicts an RBM frequency of ∼163 cm^{-1} for both tubes, in agreement with the observed value for maximum II. Similarly, the RBM intensity maximum I, at ∼136 cm^{-1}, is assigned to (23, 0) or (22, 2) tubes with near-zigzag structure. The predicted ω_{RBM} is ∼135 cm^{-1} for these two tubes. Due to the large number of possible structures and uncertainty in the measured ω_{RBM} (±2 cm^{-1}), it is practically difficult to assign a definite (n, m) structure to these low RBM frequencies. In order to assign (n, m) indices to the other observed RBM peaks between intensity maxima I and III, all possible (n, m) structures in this range within the resonance window have to be included, demonstrating that there is no preferential growth for specific nanotube structures in the CVD process.

3. **Diameter Distribution of CVD-Grown Nanotubes.** Equation 1 is used to determine the diameter of SWNTs from
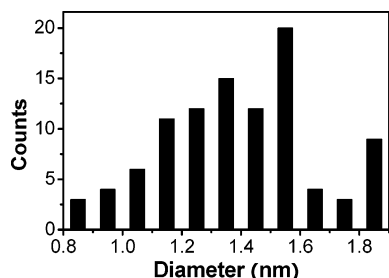
Figure 6. Distribution of diameters for 95 ultralong nanotubes determined from their RBM frequencies. The step size used to generate the histogram is 0.1 nm.
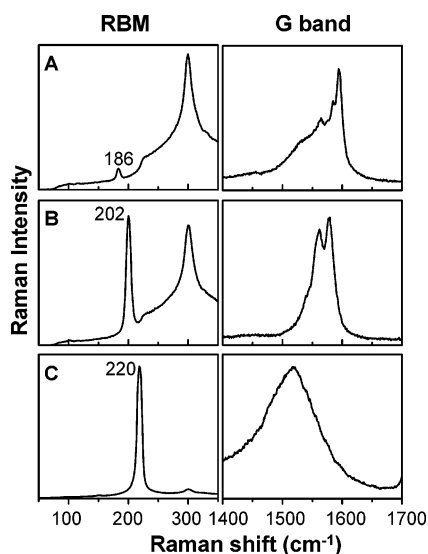

Figure 7. RBM and G-band Raman spectra for three different metallic nanotubes representing three different types of G-band Raman line shapes.

their RBM frequencies. The diameter distribution of 95 ultralong nanotubes that show RBM Raman peaks under 633-nm excitation is shown in Figure 6. The distribution peaks at $d_t = 1.5$ nm and ranges from 0.8 to 1.9 nm. A dip is observed at 1.6−1.7 nm in the diameter distribution. The diameter distribution obtained for ultralong tubes in the present study appears much broader than that previously reported for CVD-grown ultralong tubes[41] but agrees well with the diameter distribution of shorter tubes obtained in the same report.

4. **G-Band Raman Spectra of Metallic Nanotubes.** Figure 7 shows three different types of G-band Raman spectra for metallic nanotubes along with their RBM Raman spectra. In type A, the G-band consists of both a broad BWF peak and a few sharp Lorentzian peaks. The BWF peak has a full width at half-maximum (fwhm) of about 40 cm^{-1}, but the peak intensity is usually weaker than the main Lorentzian peak at ∼1590 cm^{-1}. In type C, the G-band Raman spectrum shows a broad and intense BWF feature and the sharp Lorentzian peaks are barely observable. The fwhm of the BWF peak at 1519 cm^{-1} in this case reaches 100 cm^{-1}. The B-type metallic nanotubes give a special line shape for G-band Raman spectrum, in which the BWF feature is diminished and the spectra can be fitted by a weak BWF peak and two Lorentzian peaks with fwhm of 10−20 cm^{-1}, which is broader than the typical semiconducting G-band line width (∼ 8 cm^{-1}). Most of the metallic tubes are observed to display type B G-band Raman spectra. We emphasize that the B-type G-band Raman spectra are different from typical semiconducting-type G-band Raman spectra in that the type B spectra consist of broader Lorentzians and the

components at 1590 and 1575 cm^{-1} have similar amplitudes. Our B-type G-band Raman spectrum agrees with the previously observed G-band Raman spectra for suspended freestanding metallic tubes[59] and for isolated tubes dispersed in sodium dodecyl sulfate (SDS) solution.[60]

The origin of the BWF feature in metallic G-band Raman spectra is a subject of much debate. Brown et al.[61] proposed that the BWF peak was due to coupling of the discrete tangential mode phonon (TO) to the acoustic plasmons facilitated by the nanotube curvature. Recent work involving both TEM and Raman measurement revealed that the BWF feature is enhanced in bundles but is diminished for isolated individual metallic nanotubes,[59,62] supporting an alternative mechanism proposed by Kempa[63] in which the BWF arises from phonon coupling to gapless plasmon modes that are strongly enhanced by bundle formation. However, it has been shown that the BWF feature is significantly influenced by the charge-transfer effect.[64,65] Shim et al.[65] demonstrated that the BWF feature of individual metallic nanotubes could be induced by adsorption of an electron-donating polymer, poly(ethylenimine) (PEI). Blackburn et al.[60] recently discovered that surfactants with electron-donating groups, such as cholate, tend to enhance the BWF feature for isolated tubes dispersed in surfactant solution. Our observation of diminished BWF feature for isolated metallic tubes on Si wafers in air is consistent with a very recent report by Nguyen et al.,[66] in which the B-type spectrum was attributed to O$_2$ adsorption, which causes the Fermi level shift. They also observed gradual evolution of single metallic tube G-band Raman from a narrow Lorentzian line shape to a broadened BWF line shape by shifting the Fermi level using electrochemical gating, supporting the idea that the BWF line shape is intrinsic to *single* metallic tubes but is sensitive to charge transfer.

The G-band Raman spectra of individual metallic tubes vary significantly by extrinsic factors. Samples consisting of suspended individual nanotubes across a slit on a substrate,[19] in vacuum or in an inert gas, might constitute a good system to investigate the intrinsic G-band Raman line shape for metallic tubes, which is the subject of further study.

Summary and Conclusions

We have developed a beam-scanning confocal Raman microscope that is capable of imaging single nanotubes dispersed on a large substrate surface, as is applied to characterize ultralong nanotubes grown on Si substrate by the CVD method. From comparison to SEM imaging, G-band Raman imaging with 633-nm excitation wavelength can reveal more than half (∼ 60%) of the tubes, and about half of the tubes shown in G-band Raman imaging also display RBM Raman peaks. The structural and electronic properties of nanotubes can be obtained from Raman imaging and spectroscopy. A large variation in the RBM intensity for different nanotubes is observed, which can be ascribed to different extent of resonance enhancement and structure dependence of electron−phonon coupling matrix elements. Our results show that the electron−phonon coupling involving RBM is in general weaker for nanotubes with larger diameter and larger chiral angle. A variation in the line shape of metallic G-band Raman spectra is also observed, and the BWF feature is found to be diminished in most of the isolated tubes in air, possibly due to O$_2$ adsorption.[59,65,66] The large-area imaging capability of our confocal Raman microscope, along with the nanotube structural and electronic information obtainable from Raman spectroscopy, make Raman imaging very useful in developing and fabricating nanotube-based devices with predetermined properties and behaviors.

Imaging and Raman Spectroscopy of Individual SWNTs

J. Phys. Chem. C, Vol. 111, No. 30, 2007 **11245**

References and Notes

(1) Huang, S.; Cai, X.; Liu, J. *J. Am. Chem. Soc.* **2003**, *125*, 5636.

(2) Huang, L.; Cui, X.; White, B.; O'Brien, S. P. *J. Phys. Chem. B* **2004**, *108*, 16451.

(3) Dresselhaus, M. S.; Dresselhaus, G.; Eklund, P. C. *Science of Fullerenes and Carbon Nanotubes*; Academic Press: San Diego, CA, 1996.

(4) Saito, R.; Dresselhaus, G.; Dresselhaus, M. S. *Physical Properties of Carbon Nanotubes*; Imperial College Press: London, 1998.

(5) Tans, S. J.; Verschueren, A. R. M.; Dekker, C. *Nature* **1998**, *393*, 49.

(6) Yao, Z.; Postma, H. W. C.; Balents, L.; Dekker, C. *Nature* **1999**, *402*, 273.

(7) Avouris, P. *MRS Bull.* **2004**, *29*, 403.

(8) Misewich, J. A.; Avouris, P.; Martel, R.; Tsang, J. C.; Heinze, S.; Tersoff, J. *Science* **2003**, *300*, 783.

(9) Freitag, M.; Perebeinos, V.; Chen, J.; Stein, A.; Tsang, J. C.; Misewich, J. A.; Martel, R.; Avouris, P. *Nano Lett.* **2004**, *4*, 1063.

(10) Penza, M.; Cassano, G.; Aversa, P.; Antolini, F.; Cusano, A.; Cutolo, A.; Giordano, M.; Nicolais, L. *Appl. Phys. Lett.* **2004**, *85*, 2379.

(11) Snow, E. S.; Perkins, F. K.; Houser, E. J.; Badescu, S. C.; Reinecke, T. L. *Science* **2005**, 1942.

(12) Staii, C.; Johnson, A. T.; Chen, M.; Gelperin, A. *Nano Lett.* **2005**, *5*, 1774.

(13) Sinha, N.; Ma, J.; Yeow, J. T. W. *J. Nanosci. Nanotechnol.* **2006**, *6*, 573.

(14) Heller, D. A.; Jeng, E. S.; Yeung, T.-K.; Martinez, B. M.; Moll, A. E.; Gastala, J. B.; Strano, M. S. *Science* **2006**, *311*, 508.

(15) Tsyboulski, D. A.; Bachilo, S. M.; Weisman, R. B. *Nano Lett.* **2005**, *5*, 975.

(16) Weisman, R. B.; Bachilo, S. M.; Tsyboulski, D. *Appl. Phys. A* **2004**, *A78*, 1111.

(17) Cherukuri, P.; Bachilo, S. M.; Litovsky, S. H.; Weisman, R. B. *J. Am. Chem. Soc.* **2004**, *126*, 15638.

(18) Huang, S.; Woodson, M.; Smalley, R.; Liu, J. *Nano Lett.* **2004**, *4*, 1025.

(19) Huang, L.; White, B.; Sfeir, M. Y.; Huang, M.; Huang, H. X.; Wind, S.; Hone, J.; O'Brien, S. *J. Phys. Chem. B* **2006**, *110*, 11103.

(20) Huang, S.; Maynor, B.; Cai, X.; Liu, J. *Adv. Mater.* **2003**, *15*, 1651.

(21) Guo, X.; Huang, L.; O'Brien, S.; Kim, P.; Nuckolls, C. *J. Am. Chem. Soc.* **2005**, *127*, 15045.

(22) Guo, X.; Small, J. P.; Klare, J. E.; Wang, Y.; Purewal, M. S.; Tam, I. W.; Hong, B. H.; Caldwell, R.; Huang, L.; O'Brien, S.; Yan, J.; Breslow, R.; Wind, S. J.; Hone, J.; Kim, P.; Nuckolls, C. *Science* **2006**, *311*, 356.

(23) De Poortere, E. P.; Stormer, H. L.; Huang, L. M.; Wind, S. J.; O'Brien, S.; Huang, M.; Hone, J. *Appl. Phys. Lett.* **2006**, *88*, 143124.

(24) Homma, Y.; Suzuki, S.; Kobayashi, Y.; Nagase, M.; Takagi, D. *Appl. Phys. Lett.* **2004**, *84*, 1750.

(25) Rao, A. M.; Richter, E.; Bandow, S.; Chase, B.; Eklund, P. C.; Williams, K. A.; Fang, S.; Subbaswamy, K. R.; Menon, M.; Thess, A.; Smalley, R. E.; Dresselhaus, G.; Dresselhaus, M. S. *Science* **1997**, *275*, 187.

(26) Jorio, A.; Saito, R.; Hafner, J. H.; Lieber, C. M.; Hunter, M.; McClure, T.; Dresselhaus, G.; Dresselhaus, M. S. *Phys. Rev. Lett.* **2001**, *86*, 1118.

(27) Jorio, A.; Souza Filho, A. G.; Dresselhaus, G.; Dresselhaus, M. S.; Saito, R.; Hafner, J. H.; Lieber, C. M.; Matinaga, F. M.; Dantas, M. S. S.; Pimenta, M. A. *Phys. Rev. B* **2001**, *63*, 245416/1.

(28) Yu, Z.; Brus, L. *J. Phys. Chem. B* **2001**, *105*, 1123.

(29) Saito, R.; Gruneis, A.; Samsonidze, G. G.; Brar, V. W.; Dresselhaus, G.; Dresselhaus, M. S.; Jorio, A.; Cancado, L. G.; Fantini, C.; Pimenta, M. A.; Souza Filho, A. G. *New J. Phys.* **2003**, *5*, 1.

(30) Luo, Z.; Papadimitrakopoulos, F.; Doorn, S. K. *Appl. Phys. Lett.* **2006**, *88*, 073110.

(31) Jorio, A.; Fantini, C.; Pimenta, M. A.; Heller, D. A.; Strano, M. S.; Dresselhaus, M. S.; Oyama, Y.; Jiang, J.; Saito, R. *Appl. Phys. Lett.* **2006**, *88*, 023109/1.

(32) O'Connell, M. J.; Sivaram, S.; Doorn, S. K. *Phys. Rev. B* **2004**, *69*, 235415.

(33) Doorn, S. K.; Heller, D. A.; Barone, P. W.; Usrey, M. L.; Strano, M. S. *Appl. Phys. A* **2004**, *A78*, 1147.

(34) Dresselhaus, M. S.; Dresselhaus, G.; Jorio, A.; Souza Filho, A. G.; Pimenta, M. A.; Saito, R. *Acc. Chem. Res.* **2002**, *35*, 1070.

(35) Yu, Z.; Brus, L. E. *J. Phys. Chem. B* **2001**, *105*, 6831.

(36) Souza Filho, A. G.; Chou, S. G.; Samsonidze, G. G.; Dresselhaus, G.; Dresselhaus, M. S.; An, L.; Liu, J.; Swan, A. K.; Unlu, M. S.; Goldberg, B. B.; Jorio, A.; Gruneis, A.; Saito, R. *Phys. Rev. B* **2004**, *69*, 115428/1.

(37) Pimenta, M. A.; Marucci, A.; Empedocles, S. A.; Bawendi, M. G.; Hanlon, E. B.; Rao, A. M.; Eklund, P. C.; Smalley, R. E.; Dresselhaus, G.; Dresselhaus, M. S. *Phys. Rev. B* **1998**, *58*, R16016.

(38) Kataura, H.; Kumazawa, Y.; Maniwa, Y.; Umezu, I.; Suzuki, S.; Ohtsuka, Y.; Achiba, Y. *Synth. Met.* **1999**, *103*, 2555.

(39) Jorio, A.; Souza Filho, A. G.; Dresselhaus, G.; Dresselhaus, M. S.; Swan, A. K.; Unlu, M. S.; Goldberg, B. B.; Pimenta, M. A.; Hafner, J. H.; Lieber, C. M.; Saito, R. *Phys. Rev. B* **2002**, *65*, 155412/1.

(40) Jiang, C.; Zhao, J.; Therese, H. A.; Friedrich, M.; Mews, A. *J. Phys. Chem. B* **2003**, *107*, 8742.

(41) Doorn, S. K.; Zheng, L.; O'Connell, M. J.; Zhu, Y. T.; Huang, S.; Liu, J. *J. Phys. Chem. B* **2005**, *109*, 3751.

(42) Doorn, S. K.; O'Connell, M. J.; Zheng, L.; Zhu, Y. T.; Huang, S.; Liu, J. *Phys. Rev. Lett.* **2005**, *94*, 016802.

(43) Son, H.; Reina, A.; Samsonidze, G. G.; Saito, R.; Jorio, A.; Dresselhaus, M. S.; Kong, J. *Phys. Rev. B* **2006**, *74*, 073406/1.

(44) Anderson, N.; Anger, P.; Hartschuh, A.; Novotny, L. *Nano Lett.* **2006**, *6*, 744.

(45) Jorio, A.; Souza Filho, A. G.; Brar, V. W.; Swan, A. K.; Unlu, M. S.; Goldberg, B. B.; Righi, A.; Hafner, J. H.; Lieber, C. M.; Saito, R.; Dresselhaus, G.; Dresselhaus, M. S. *Phys. Rev. B* **2002**, *65*, 121402/1.

(46) Duesberg, G. S.; Loa, I.; Burghard, M.; Syassen, K.; Roth, S. *Phys. Rev. Lett.* **2000**, *85*, 5436.

(47) Jorio, A.; Dresselhaus, G.; Dresselhaus, M. S.; Souza, M.; Dantas, M. S. S.; Pimenta, M. A.; Rao, A. M.; Saito, R.; Liu, C.; Cheng, H. M. *Phys. Rev. Lett.* **2000**, *85*, 2617.

(48) Samsonidze, G. G.; Saito, R.; Kobayashi, N.; Grueneis, A.; Jiang, J.; Jorio, A.; Chou, S. G.; Dresselhaus, G.; Dresselhaus, M. S. *Appl. Phys. Lett.* **2004**, *85*, 5703.

(49) Son, H. B.; Reina, A.; Dresselhaus, M. S.; Kong, J. *Phys. Status Solidi B* **2006**, *243*, 3161.

(50) Saito, R.; Dresselhaus, G.; Dresselhaus, M. S. *Phys. Rev. B* **2000**, *61*, 2981.

(51) Strano, M. S. *J. Am. Chem. Soc.* **2003**, *125*, 16148.

(52) Telg, H.; Maultzsch, J.; Reich, S.; Hennrich, F.; Thomsen, C. *Phys. Rev. Lett.* **2004**, *93*, 177401.

(53) Araujo, P. T.; Doorn, S. K.; Kilina, S.; Tretiak, S.; Einarsson, E.; Maruyama, S.; Chacham, H.; Pimenta, M. A.; Jorio, A. *Phys. Rev. Lett.* **2007**, *98*, 067401.

(54) Maultzsch, J.; Telg, H.; Reich, S.; Thomsen, C. *Phys. Rev. B* **2005**, *72*, 205438.

(55) Meyer, J. C.; Paillet, M.; Michel, T.; Moreac, A.; Neumann, A.; Duesberg, G. S.; Roth, S.; Sauvajol, J.-L. *Phys. Rev. Lett.* **2005**, *95*, 217401.

(56) Yin, Y.; Vamivakas, A. N.; Walsh, A. G.; Cronin, S. B.; Unlu, M. S.; Goldberg, B. B.; Swan, A. K. *Phys. Rev. Lett.* **2007**, *98*, 037404.

(57) Goupalov, S. V.; Satishkumar, B. C.; Doorn, S. K. *Phys. Rev. B* **2006**, *73*, 115401.

(58) Popov, V. N.; Henrard, L.; Lambin, P. *Phys. Rev. B* **2005**, *72*, 035436.

(59) Paillet, M.; Poncharal, P.; Zahab, A.; Sauvajol, J.-L. *Phys. Rev. Lett.* **2005**, *94*, 237401.

(60) Blackburn, J. L.; Engtrakul, C.; McDonald, T. J.; Dillon, A. C.; Heben, M. J. *J. Phys. Chem. B* **2006**, *110*, 25551.

(61) Brown, S. D. M.; Jorio, A.; Corio, P.; Dresselhaus, M. S.; Dresselhaus, G.; Saito, R.; Kneipp, K. *Phys. Rev. B* **2001**, *63*, 155414/1.

(62) Jiang, C.; Kempa, K.; Zhao, J.; Schlecht, U.; Kolb, U.; Basche, T.; Burghard, M.; Mews, A. *Phys. Rev. B* **2002**, *66*, 161404.

(63) Kempa, K. *Phys. Rev. B* **2002**, *66*, 195406.

(64) Yu, Z.; Brus, L. E. *J. Phys. Chem. A* **2000**, *104*, 10995.

(65) Shim, M.; Ozel, T.; Gaur, A.; Wang, C. *J. Am. Chem. Soc.* **2006**, *128*, 7522.

(66) Nguyen, K. T.; Gaur, A.; Shim, M. *Phys. Rev. Lett.* **2007**, *98*, 145504.